**Proceedings of the ASME 2023 42nd International
Conference on Ocean, Offshore and Arctic Engineering
OMAE2023
June 11-16, 2023, Melbourne, Australia**

OMAE2023-105249

STOCHASTIC VORTEX-INDUCED VIBRATION IN FREE-STREAM TURBULENCE USING A PHENOMENOLOGICAL MODEL

Rameez Badhurshah [1]**, Narakorn Srinil**[1]**, John R. Chaplin**[2]**, Philipp Thies**[3]**, Lars Johanning**[3]**,
Alistair G.L. Borthwick**[4]**, Vengatesan Venugopal**[4]

[1]Newcastle University, Newcastle upon Tyne, UK, [2]University of Southampton, Southampton, UK
[3]University of Exeter, Exeter, UK, [4]University of Edinburgh, Edinburgh, UK

ABSTRACT

Underwater dynamic power cables connected to offshore floating energy devices are subject to ocean turbulence and, through eddy shedding, may experience vortex-induced vibration (VIV). A high level of turbulence intensity may cause fatigue damage to cables in the ocean. The present preliminary study investigates the VIV response of a rigid circular cylinder in free-stream turbulent flow. A phenomenological reduced-order wake oscillator model is coupled with a stochastic differential equation that represents flow turbulence. The model consists of two coupled ordinary differential equations: one, a structure oscillator equation that considers forcing from the vortex shedding wake; the other, a van der Pol oscillator with a structural coupling term. Wake oscillator models have been used extensively in the past, with many application-specific versions having been developed. The stochastic differential equation accounts for random fluctuations in the fluid flow velocity. Here, we vary the turbulence intensity in the model up to a maximum of 20%. The cylinder response is not significantly affected by very low levels of turbulence, but amplitude modulations and beating phenomena are observed in a strongly turbulent flow. Lock-in, whereby the structure oscillation frequency synchronizes with the vortex shedding frequency, is also explored to study how the resonant frequencies differ in cases with and without turbulence present. We also investigate the stochastic VIV response of a cable structure to changes in mass-damping ratio, fluid-structure coupling terms, and initial conditions. The findings should be of benefit to researchers and design engineers concerned with the development of floating energy systems by better characterizing operational load conditions for new installations.

1 INTRODUCTION

Underwater cables connected to offshore floating wind energy devices can experience vortex-induced vibrations (VIV) as the cable interacts with the ocean flow and vortex shedding occurs [1, 2]. Owing to repetitive loading in the turbulent oceanic environment, an underwater cable experiences fatigue. Extreme weather, and adverse operating and environmental conditions may amplify oceanic turbulence, causing an underwater cable to become damaged. To design cables so that they are resilient, it is important first to understand the likely response of a cable immersed in free-stream turbulence [3].

Numerous experimental and numerical studies have considered fixed cylinders experiencing VIV in water and air (see e.g., [4]). In the last two decades, increasing research effort has been directed towards the study of flexible cylinders experiencing VIV, partly driven by an interest in energy generation from VIV as part of the response to the world's energy crisis [5, 6]. However, the effect of free-stream turbulence on the stochastic VIV of a cable/rigid cylinder has been relatively little explored except for a few recent studies (see [7–10]).

Phenomenological models such as the wake oscillator model (WOM) can be useful to predict the stochastic response of cables subject to free-steam turbulence [11, 12]. WOM essentially

comprises two coupled ordinary differential equations. The first equation models the equation of motion of the structure with a forcing term from the fluid, while the second equation comprises the wake equation of motion incorporating a forcing term from the structure. WOMs capture many features of the responsive behaviour; they are fast to run and much less computationally expensive than computational fluid dynamics (CFD) models [13].

In the present study, the WOM proposed by Nielsen and Krenk [14,15] is used to mimic the stochastic response. To avoid the design complexity involved with a flexible cable, we consider a simple rigid cylindrical structure of circular cross-section that experiences VIV in a turbulent environment. The forcing terms of both equations in this model use the concept of an exact balance of energy exchange taking place between the fluid and the structure. This implies that, at all times, the forcing terms are fed with exactly the same energy flow. The model is exploited to predict the response behaviour for two different mass ratios at different turbulence intensities.

2 STOCHASTIC WAKE-CYLINDER OSCILLATORS
2.1 Structure oscillator
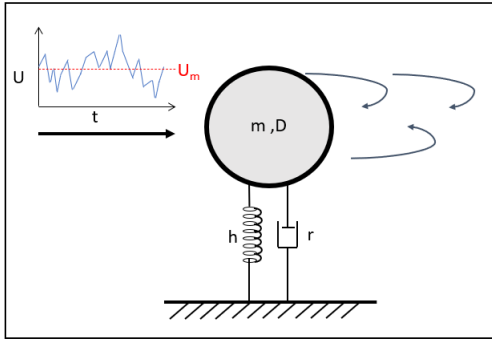
FIGURE 1: SCHEMATIC MODEL OF A CYLINDER-SPRING-DAMPER SYSTEM IN TURBULENT FLOW.

We consider the two-dimensional problem of a spring-mounted rigid cylinder of diameter D and mass m attached to linear springs of stiffness h and damping constant r placed in the fluid of density ρ and uniform fluid velocity U (Fig. 1). Here, the fluid velocity U can be expressed as $U = U_m + u(t)$, where U_m is the mean flow velocity and $u(t)$ is the turbulent velocity component [7, 8, 15]. The cylinder experiences vibrations in the cross-flow direction due to its interaction with the fluid flow. The equation of motion of the cylinder may be written,

$$m\ddot{Y} + r\dot{Y} + hY = \frac{1}{2}\rho U^2 D C_L \qquad (1)$$

where Y is the instantaneous transverse displacement of the cylinder and C_L is the lift coefficient which is expressed in terms of the wake displacement Q and wake coupling coefficient γ as $C_L = \frac{\dot{Q}(t)}{U}\gamma$ in which t is time. Following Nielsen and Krenk [15],

we replace $\mu_0 = \frac{\rho D^2 l}{m}$ and non-dimensionalize the resulting equation by setting $y = Y/D, \dot{y} = \dot{Y}/D, \ddot{y} = \ddot{Y}/D, q = Q/Q_0, \dot{q} = \dot{Q}/Q_0$ and $\ddot{q} = \ddot{Q}/Q_0$. Here, y and its resulting equation become

$$\ddot{y} + 2\xi\omega\dot{y} + \omega^2 y = \mu_0 c_0 \omega_f \dot{q} \qquad (2)$$

where ω is the structural frequency, U_r is the reduced velocity and $c_0 = Q_0\gamma/4\pi St$ is the non-dimensional coupling parameter in which St is the Strouhal number. To take into account the effects of turbulence, the reduced velocity is expressed as $U_r = U_r(1 + R(t))$, where $R(t) = 2u(t)/U_m$ is the stochastic turbulence process. Here $u(t)$ is the local fluctuating velocity component and U_m is the mean flow speed. $R(t)$ takes the form of mean reverting Ornstein-Uhlenbeck process [15], which can be simulated from the Ito-differential equation:

$$dR(t) = -\frac{1}{\tau_c}R(t)dt + \sqrt{\frac{2}{\tau_c}}\sigma_R dW(t) \qquad (3)$$

In the above equation, τ_c is the correlation time scale, σ_R is the standard deviation which relates to the turbulent intensity (I_u) defined by the expression $I_u = \frac{1}{2}\sigma_R$ based on the definition of R(t) [15], and $dW(t)$ is the standard Weiner process. A more general and accepted way of defining turbulence intensity is as the ratio of the standard deviation of the turbulent velocity component to the mean flow velocity component. The above differential equation is solved numerically using the Euler-Maruyama method [16]. The structure oscillator with a stochastic turbulence process is given by

$$\ddot{y} + 2\xi\omega\dot{y} + \omega^2 y = (1 + R)\mu_0 c_0 \omega_f \dot{q} \qquad (4)$$

where ω_f is the fluid oscillator frequency.

2.2 Wake oscillator

As the model is based on the principle of energy balance between the forcing terms of the structure and wake, the wake oscillator receives the same energy in its forcing terms as the structure oscillator. The equation is thus given by

$$m_f\ddot{Q} - 2m_f\varepsilon\omega_f(1 - \frac{(Q^2 + \dot{Q}^2/\omega_f^2)}{Q_0^2})\dot{Q} + m_f\omega_f^2 Q$$
$$= -\frac{1}{2}\rho U^2 D \frac{\dot{Y}(t)}{U}\gamma \qquad (5)$$

where m_f is the fluid mass, ε is the wake coupling coefficient and ω_f is the fluid oscillator frequency defined as $\omega_f = 2\pi St U/D$. St is the Strouhal number and in the present study, we use $St = 0.2$. The above equation is non-dimensionalized in the same way as previously for the structure oscillator equation, giving:

$$\ddot{q} - 2\varepsilon\omega_f(1 - q^2 - \frac{\dot{q}^2}{\omega_f^2})\dot{q} + \omega_f^2 q = -c_0 v_0^{-2}\omega_f\dot{y} \qquad (6)$$

where v_0 is the normalized amplitude of the fluid oscillator on a fixed cylinder in laminar flow. Next, the effect of turbulence

TABLE 1: MAIN INPUT PARAMETERS AND VALUES IN EQS. 4 AND 7.

Parameter	Symbol	Value
Mass ratio	$m^* = \frac{m}{\frac{\pi}{4}\rho D^2 l}$	2.54 and 12.73
Structural damping	ξ	$1.25E - 03$
Turbulence intensity	I_u	5%, 10%, 20%
Strouhal number	St	0.2
Coupling coefficient	A	0.177 ($m^* = 2.54$)
Coupling coefficient	A	0.0035 ($m^* = 12.73$)
Wake damping coefficient	ε	0.064

is added to the above equation. The coupling coefficient is expressed in simple terms as $c_0 v_0^{-2} = A$. The wake oscillator accounting for turbulence is then expressed as,

$$\ddot{q} - 2\varepsilon(1 - q^2 - \frac{\dot{q}^2}{\omega_f})\omega_f \dot{q}$$
$$+ \omega_f^2 (1 + R)^2 q = -A\omega_f (1 + R)\dot{y} \tag{7}$$

Eqs. 4 and 7 are the same as those used in [15]. In the present simulations, to obtain the range of different reduced velocities, the natural frequency ω_0 is varied while the vortex shedding frequency ω_f is kept constant, to obtain the corresponding reduced velocity. The solution for the stochastic wake oscillator is obtained by solving Eq. 3 using the Euler-Maruyama method and then incorporating the solution at each time step in Eqs. 4 and 7 and in the time integration.

2.3 Parametric consideration

Table 1 lists values of key constants and parameters used in the simulations. The mass ratios are selected based on a preliminary literature review of VIV experiments of circular cylinders with low mass ratios ranging between $2 \le m^* \le 20$ [17]. Values of the Strouhal number and coupling coefficients have been adopted from those given by Nielsen and Krenk [15]. Note that the coupling coefficients need to be tuned and are presently dependent on the mass ratio.
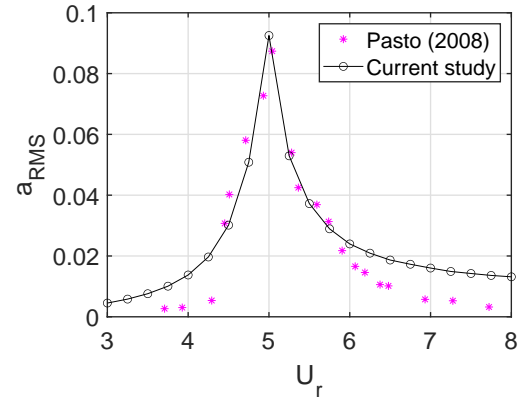
2.4 Validation

In this section, we validate the present model using existing experimental data. Firstly, in Fig. 2, the model prediction results for the maximum amplitude normalized with respect to D (a_0) are validated against experimental VIV results for a circular cylinder with a low mass ratio of $m^* = 2.4$ and low damping ratio $\xi = 0.00542$. For this low mass ratio, the coupling coefficients are similar to those reported in Table 1 for $m^* = 2.54$.

Next, in Fig. 3, we compare predicted results for the nondimensionalized root-mean-squared (RMS) amplitude, $a_{RMS} = \frac{Y_{RMS}}{D}$, against experimental data for VIV of a cylinder in uniform flow with low turbulence intensity [18]. In the literature, to the best of the authors' knowledge, experimental results for VIV of cylinders with low mass ratios in free-stream turbulent flows are limited. Hence, we consider experimental data that are available for a high mass ratio case with $m^* = 133.75$. In both validation cases, the model is found to give predictions that compare well with observed maximum responses. In the latter case, the amplitude response is low primarily because of the high mass ratio. Note that the Strouhal number adopted for the validation is $St = 0.2095$ and the coupling coefficients (associated with the mass ratio) are $c_0 = 1.473$ and $A = 6.788$ on tuning the model.
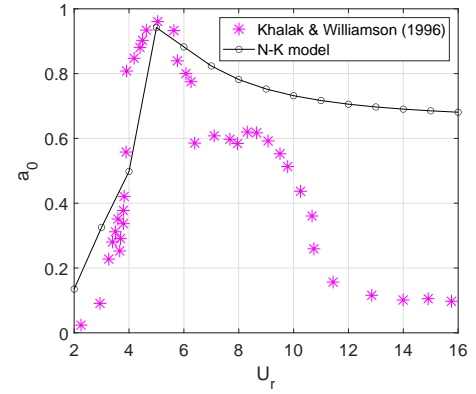
FIGURE 2: MODEL VALIDATION AGAINST EXPERIMENTAL DATA [17] FOR CYLINDER VIV WITH A LOW MASS RATIO ($m^* = 2.4$).

FIGURE 3: MODEL VALIDATION AGAINST EXPERIMENTAL DATA [18] FOR VIV IN TURBULENT FLOW ($m^* = 133.75$, $I_u = 3\%$ and $\xi = 3.9E - 03$.)

3 RESULTS AND DISCUSSION

Eqs. 4, 7 and 3 have been solved in MATLAB for two sets of mass ratios by considering the turbulence-free flow vs. the free-stream flow with low, medium, and high turbulence intensities.

First, we present a_{RMS} versus the reduced velocity for each of the mass ratios 2.54 and 12.73, and for different turbulent intensities. Low mass ratios are considered in order to mimic actual underwater systems. We then discuss the power spectral density (PSD) contour plots for each case. The simulations have been performed by increasing and decreasing the reduced velocity parameter. The first case run in each set is initiated with an initial displacement of $y_0 = 0.1$. The rms values from the first reduced velocity case are used as inputs to initiate the second or next reduced velocity case. This cycle is repeated until the last reduced velocity has been considered.

3.1 Response amplitudes
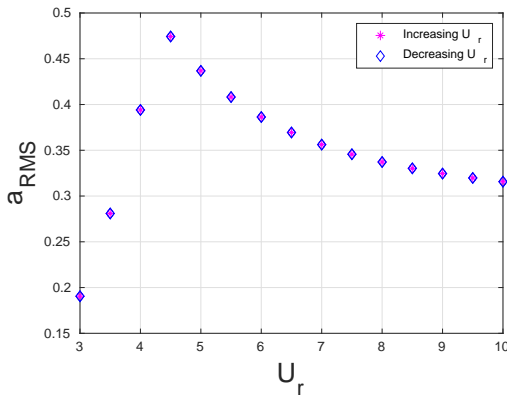
FIGURE 4: VARIATION IN RMS AMPLITUDES WITH U_r FOR $m^* = 2.54$ AND ZERO TURBULENCE.
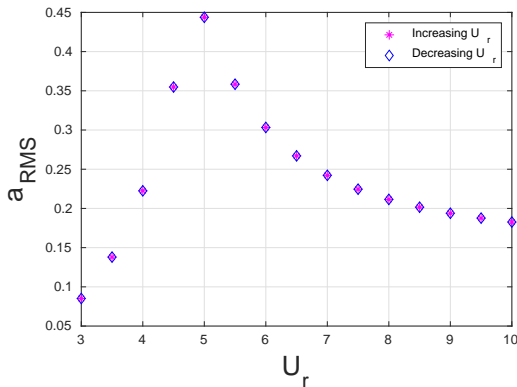
FIGURE 5: VARIATION IN RMS AMPLITUDES WITH U_r FOR $m^* = 12.73$ AND ZERO TURBULENCE.

3.1.1 No turbulence intensity: Figs 4 and 5 show the variation of rms amplitude plotted against reduced velocity in the absence of turbulence intensity for $m^* = 2.54$ and $m^* = 12.73$ respectively. In both cases, the rms amplitude is small when $U_r < 4$, corresponding to the lower branch. The amplitude then rises to a peak at $U_r = 4.5$ for $m^* = 2.54$ and at $U_r = 5$ for $m^* = 12.73$. This zone represents lock-in where the structure frequency synchronizes with the fluid frequency, and is termed the upper branch. The amplitude then falls steadily until $U_r = 10$. Even so, there is no significant drop in amplitude observed and so the branch still corresponds to the upper branch. Similar response amplitudes and features between the increasing U_r and decreasing U_r cases suggest the negligible hysteresis effect. The trend observed in the current results matches qualitatively with wind tunnel experiments performed by Pasto for higher mass ratios [18].
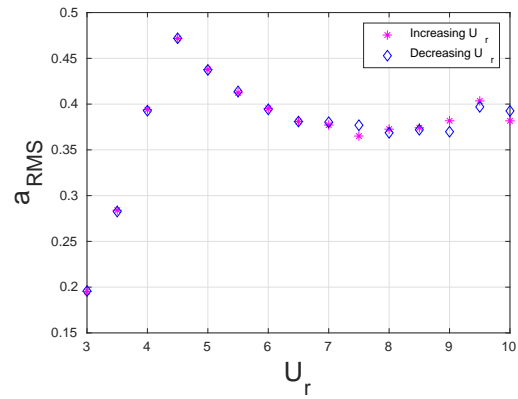

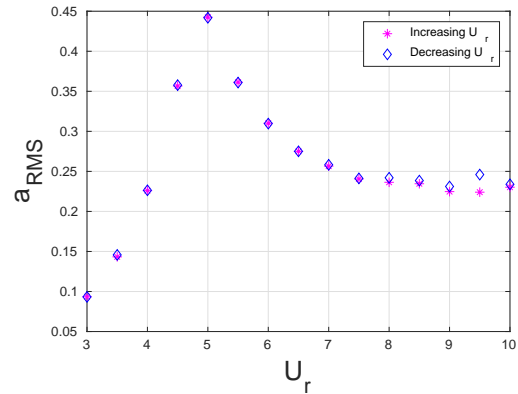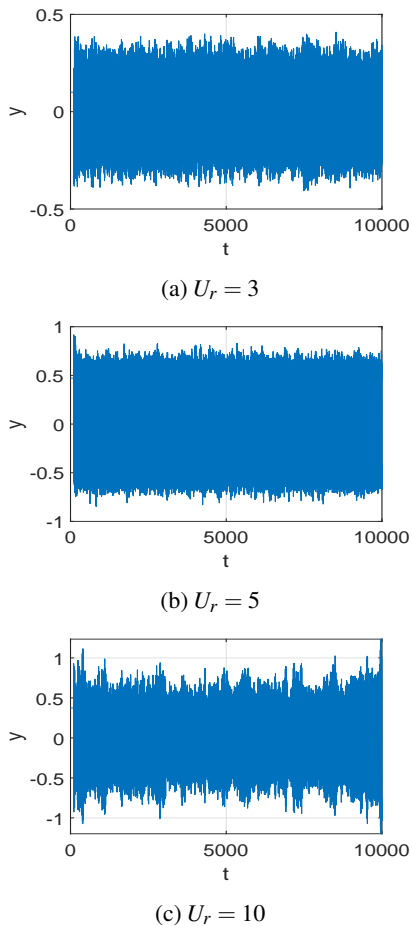**FIGURE 6**: VARIATION IN RMS AMPLITUDES WITH U_r FOR $m^* = 2.54$ AND $I_u = 5\%$.

FIGURE 7: VARIATION IN RMS AMPLITUDES WITH U_r FOR $m^* = 12.73$ AND $I_u = 5\%$.

3.1.2 Low turbulence intensity ($I_u = 5\%$): As defined previously, turbulence intensity is the ratio of the standard deviation of the turbulent velocity component to the mean flow velocity component. Figs 6 and 7 show the variation in rms

amplitude with reduced velocity for both mass ratios at 5% turbulence intensity. The results display similar qualitative trends for the no turbulence case for reduced velocity in the range $3 \leq U_r \leq 7$. At higher U_r, we observe larger amplitudes than in the corresponding cases with no turbulence. To investigate this further, we plot the time histories of displacement and the phase portrait at $U_r = 3, 5, 9$ for $m^* = 2.54$ in Fig. 8 and Fig. 9 respectively. These two figures show that signal modulation is significant at higher reduced velocities due to the existence of a stochastic process in the signal. Near the lock-in zone, the signal remains smooth and no chaotic signal is observed. The trends for $m^* = 12.73$ at $I_u = 5\%$ are similar.

(a) $U_r = 3$

(b) $U_r = 5$

(c) $U_r = 10$

FIGURE 8: $I_u = 5\%$ TIME SERIES FOR $m^* = 2.54$ AND $U_r = 3$ (pre lock-in), $U_r = 5$ (lock-in), and $U_r = 10$ (far lock-in) .

3.1.3 Medium turbulence intensity ($I_u = 10\%$): Figs 10 and 11 show the variation in rms amplitude with reduced velocity for both mass ratios and a turbulence intensity of 10%. Interestingly, we observe an increment in amplitude over the entire range of reduced velocities for each of the mass ratios when compared to the respective mass ratio cases of low turbulence intensity respectively. Beyond $U_r \geq 8$, a further increase


(a) $U_r = 3$

(b) $U_r = 5$

(c) $U_r = 10$
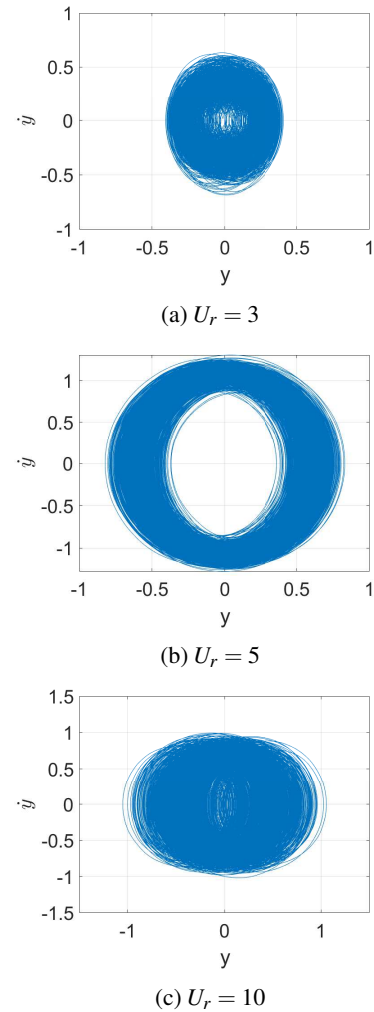
FIGURE 9: $I_u = 5\%$ PHASE PORTRAITS FOR $m^* = 2.54$ AND $U_r = 3$ (pre lock-in), $U_r = 5$ (lock-in) and $U_r = 10$ (far lock-in) .

in rms amplitude results from the components at higher frequencies becoming dominant over those at the structural frequency. Fig. 12 shows the time series and corresponding phase portrait for $m^* = 2.54$ and $U_r = 4$. A chaotic signal and a sudden jump in amplitude occur. The presence of dual amplitudes can be discerned from the phase portrait. The jump occurs when one of the frequencies of the chaotic signal synchronizes with the fluid frequency.

3.1.4 With high turbulence intensity ($I_u = 20\%$) We next consider a higher value of turbulence intensity of 20%. Figs 13 and 14 show the variation in rms amplitudes with the reduced velocity for each of the two mass ratios. The trends obtained for the two mass ratios differ significantly. For low m^*, the amplitude increases progressively with reduced velocity. Significantly larger amplitudes are observed, perhaps due to incorrect tuning of the coupling coefficients. For $m^* = 12.73$, the rms am-

5
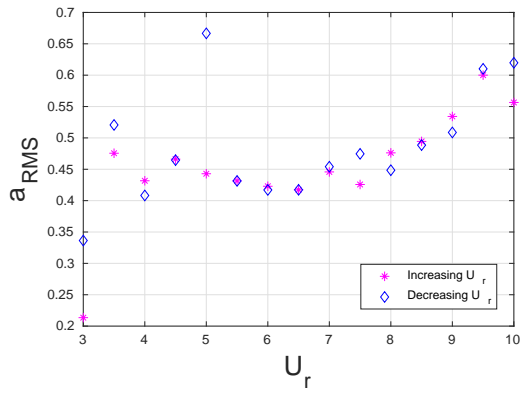
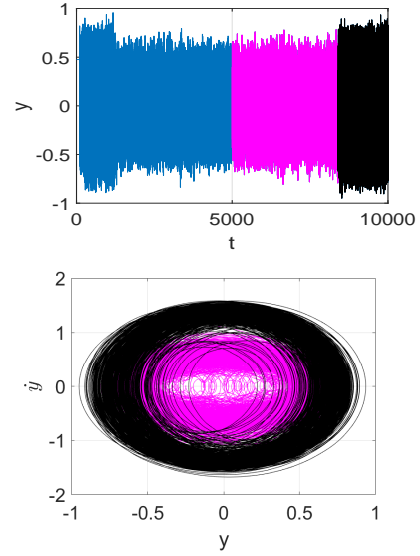**FIGURE 10**: VARIATION IN RMS AMPLITUDES WITH U_r FOR $m^* = 2.54$ AND $I_u = 10\%$.
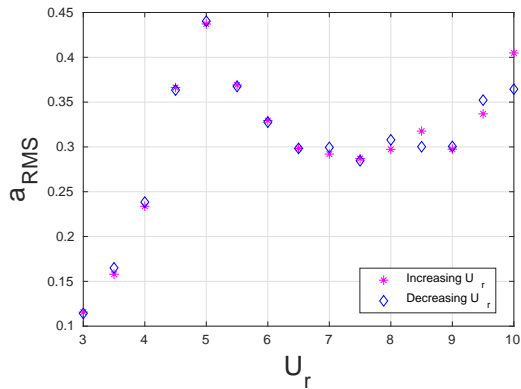
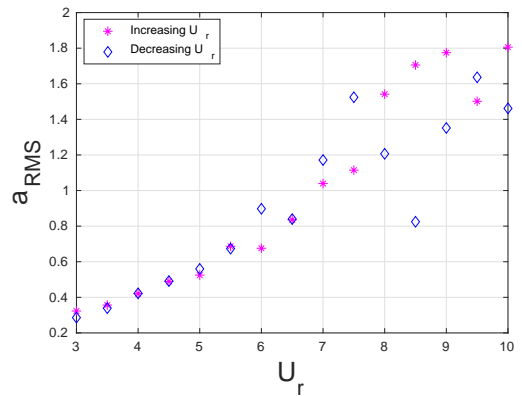**FIGURE 11**: VARIATION IN RMS AMPLITUDES WITH U_r FOR $m^* = 12.73$ AND $I_u = 10\%$.

plitude increases to $U_r \approx 5.5$, drops significantly at $U_r = 5$, and then increases steadily. This trend remains similar for both increasing and decreasing reduced velocity simulations. Chaos exists in the signal, as exemplified by Fig. 15. Dual amplitude responses are evident and the signal remains chaotic throughout the simulation. In the time series and phase portrait plots, a colour coding is used to distinguish between the amplitude branches.

3.2 Response frequencies

Response frequencies with the power spectral density (PSD) contour plots are now presented, with the reduced velocity on the abscissa and the frequency on the ordinate axis. At each frequency, the power spectrum is plotted vertically and the results are combined horizontally over the range of reduced velocity $3 \leq U_r \leq 10$. Here, the log_{10} scale is used to contrast the variation, with blue representing -10 and red indicating 0. Each contour plot is superimposed with the natural frequency in vacuum nondimensionalized with respect to the vortex shedding frequency.
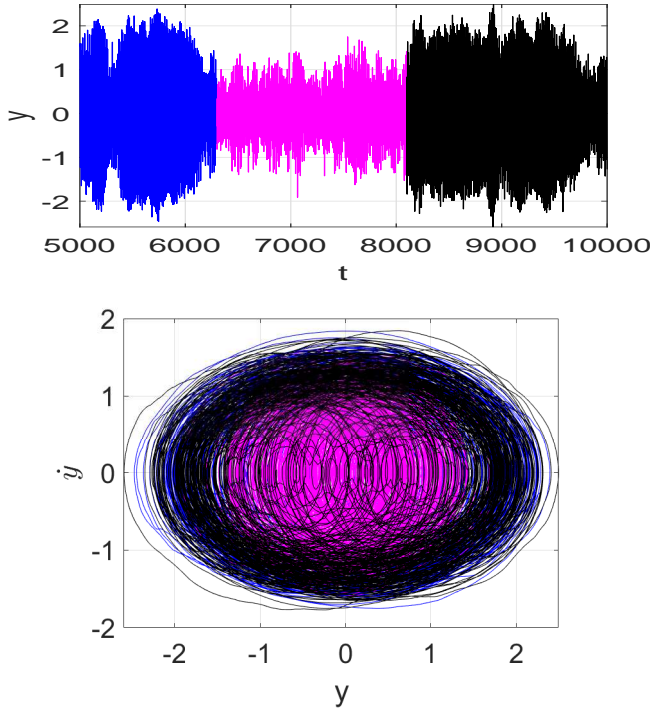

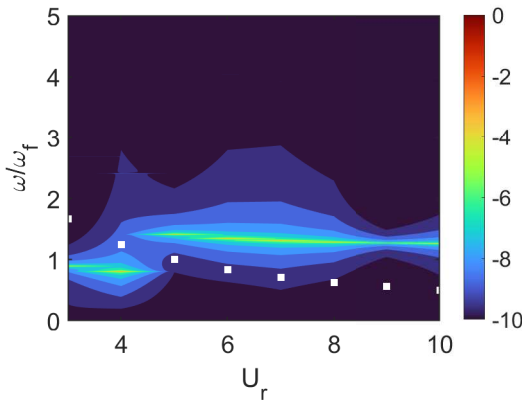**FIGURE 12**: $I_u = 10\%$ TIME SERIES AND PHASE PORTRAIT FOR $m^* = 2.54$ AND $U_r = 4$.

FIGURE 13: VARIATION IN RMS AMPLITUDES WITH U_r FOR $m^* = 2.54$ AND $I_u = 20\%$.
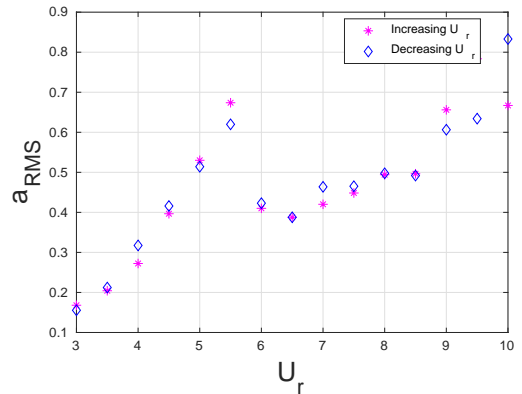
**FIGURE 14**: VARIATION IN RMS AMPLITUDES WITH U_r FOR $m^* = 12.73$ AND $I_u = 20\%$.

6

FIGURE 15: $I_u = 20\%$ TIME SERIES AND PHASE POR-TRAITS FOR $m^* = 2.54$ AND $U_r = 7$.

FIGURE 16: PSD CONTOUR PLOT FOR $m^* = 2.54$ WITH ZERO TURBULENCE. A WHITE MARKER REPRESENTS THE NATURAL FREQUENCY IN VACUUM FOR THAT CORRESPONDING REDUCED VELOCITY.
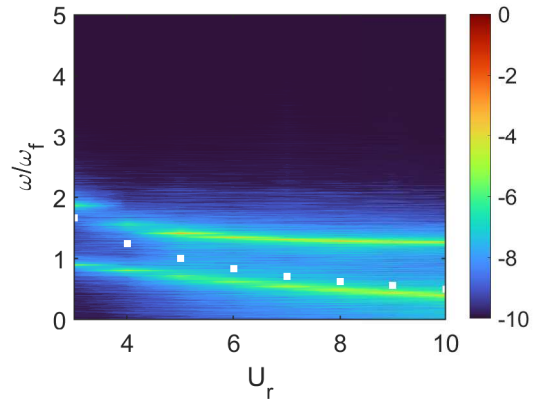
3.2.1 No turbulence intensity
Figs 16 and 17 show the PSD contour plots for $m^* = 2.54$ and 12.73 in the absence of turbulence. A shift in frequency is observed at particular U_r in both the PSD plots. For $m^* = 2.54$ the shift in frequency occurs at $U_r = 4.5$ while for $m^* = 12.73$, the shift in frequency occurs at $U_r = 5$. This shift in frequency accounts for two separate zones. These zones correspond to the initial and the upper lock-in branch, as discussed earlier. Lock-in between structure
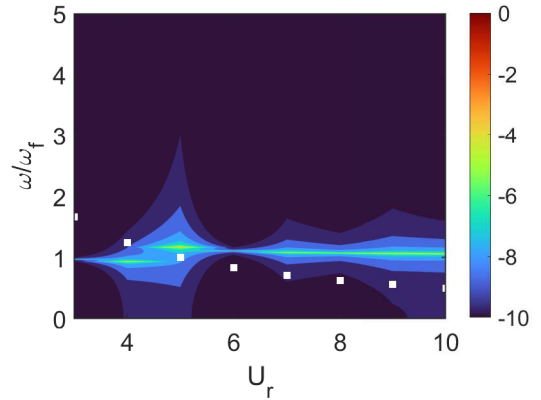
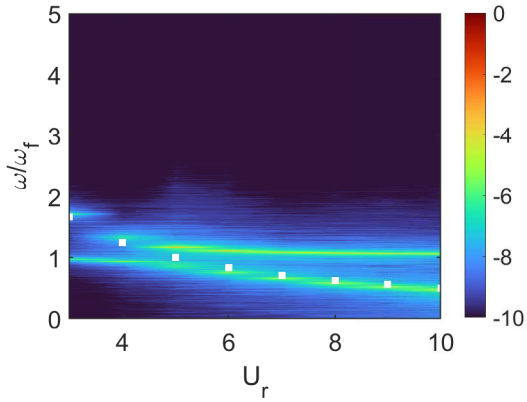FIGURE 17: PSD CONTOUR PLOT FOR $m^* = 12.73$ WITH ZERO TURBULENCE.

and natural frequency occurs for cases of lower reduced velocity whereas the structure locks in with the vortex shedding frequency at higher reduced velocity.

3.2.2 Low turbulence intensity ($I_u = 5\%$)
Figs 18 and 19 display the PSD contours for 5% turbulence intensity at each mass ratio. Two different frequencies are observed beyond $U_r = 5$ indicating the presence of other harmonics, arising from the stochastic process in the flow.
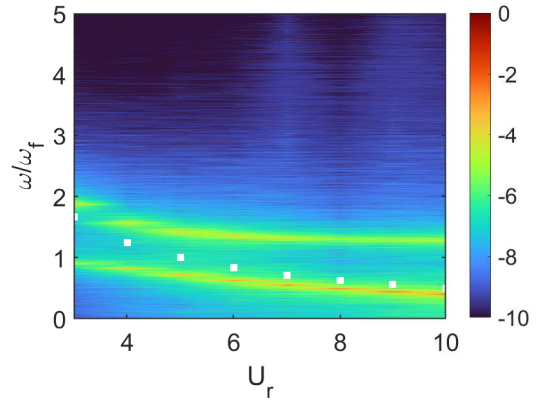

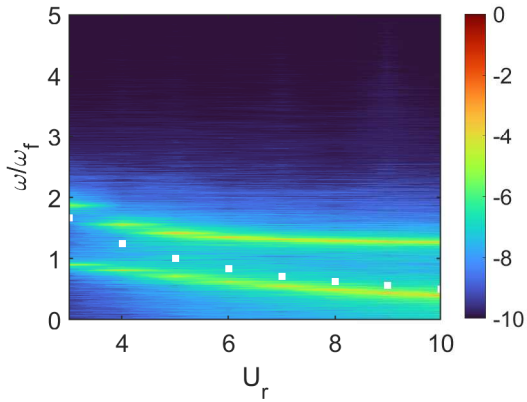FIGURE 18: PSD CONTOUR PLOT FOR $m^* = 2.54$ AND $I_u = 5\%$.

3.2.3 Medium and high turbulence intensity ($I_u = 10\%$ & 20%)
Figs 20 and 22 show PSD contour plots obtained for 10% and 20% turbulence intensity for $m^* = 2.54$. Figs 21 and 23 show the PSD contours for the same turbulence intensities for $m^* = 12.73$. The presence of dual frequencies is observed even at the higher level of turbulence intensity. The two frequencies correspond to the vortex shedding frequency and the natural frequency, respectively. As the turbulence intensifies, the natural frequency signals correspond to higher power spectrum values compared to the vortex shedding frequency. This is in agreement
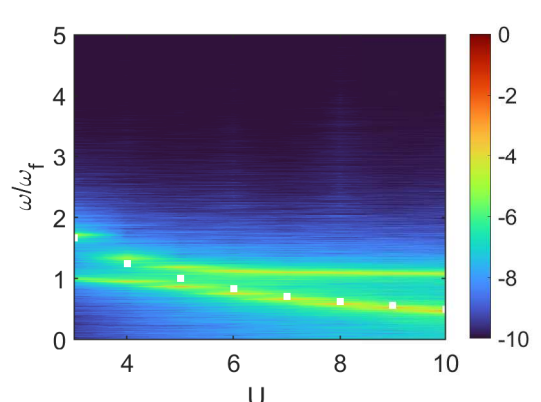
7

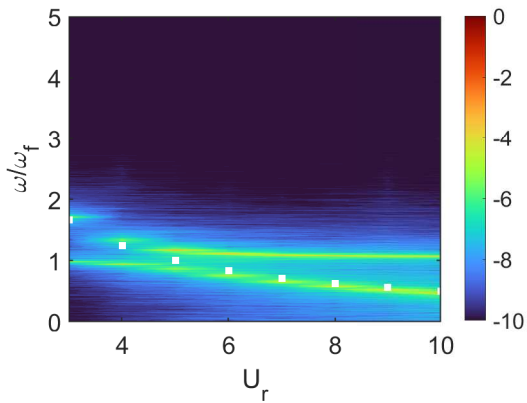**FIGURE 19**: PSD CONTOUR PLOT FOR $m^* = 12.73$ AND $I_u = 5\%$.

FIGURE 20: PSD CONTOUR PLOT FOR $m^* = 2.54$ AND $I_u = 10\%$.

FIGURE 21: PSD CONTOUR PLOT FOR $m^* = 12.73$ AND $I_u = 10\%$.

with the dual amplitudes in Fig 15 where the structure can select to lock into either the vortex shedding or natural frequency.

FIGURE 22: PSD CONTOUR PLOT FOR $m^* = 2.54$ AND $I_u = 20\%$.

FIGURE 23: PSD CONTOUR PLOT FOR $m^* = 12.73$ AND $I_u = 20\%$.

The results presented are part of a preliminary study using a phenomenological model. We intend to improve the model with the laboratory scale data in the near future.

4 CONCLUSION

This paper presents a modified wake oscillator model and results from a preliminary numerical study that has assessed the response of a circular cylinder placed in free-stream turbulent flow and undergoing VIV. Two different mass ratios, $m^* = 2.54$ and 10.73, and the turbulence intensity up to 20% have been considered. Results show that VIV response amplitudes increase with the increasing turbulence intensity but reduce with the higher mass ratio. Chaotic response signals are observed in a high turbulence intensity case. For each of the reduced velocities considered, two separate branches are observed in the response frequency spectra for turbulent flow cases. Frequencies for the VIV lock-in conditions correspond to the considerably larger peaks in the power spectra when a stronger turbulence intensity is present.

5 ACKNOWLEDGEMENT

NOMENCLATURE

A	wake coupling coefficient
a_0	nondimensional maximum amplitude
a_{RMS}	nondimensional RMS amplitude
C_L	lift coefficient
c_0	coupling parameter
D	cylinder diameter
h	spring stiffness
I_u	turbulent intensity
m	cylinder mass
m_f	displaced fluid mass
m^*	mass ratio
Q	dimensional wake variable
$R(t)$	stochastic turbulence process
r	damping coefficient
St	Strouhal number
U	fluid velocity
U_m	mean flow velocity
U_r	reduced velocity
$u(t)$	turbulent velocity component
Y	dimensional cylinder displacement
y	nondimensional cylinder displacement
ε	wake coupling coefficient
ξ	damping ratio
ρ	fluid density
σ_R	standard deviation
τ_c	correlation time scale
ω	structural frequency
ω_f	fluid oscillator frequency

REFERENCES

[1] Williamson, C., and Govardhan, R., 2008. "A brief review of recent results in vortex-induced vibrations". *Journal of Wind Engineering and Industrial Aerodynamics, 96*(6-7), pp. 713–735.

[2] Brika, D., and Laneville, A., 1993. "Vortex-induced vibrations of a long flexible circular cylinder". *Journal of Fluid Mechanics, 250*, pp. 481–508.

[3] Bearman, P., and Morel, T., 1983. "Effect of free stream turbulence on the flow around bluff bodies". *Progress in Aerospace Sciences, 20*(2-3), pp. 97–123.

[4] Williamson, C. H., Govardhan, R., et al., 2004. "Vortex-induced vibrations". *Annual Review of Fluid Mechanics, 36*(1), pp. 413–455.

[5] Evangelinos, C., and Karniadakis, G. E., 1999. "Dynamics and flow structures in the turbulent wake of rigid and flexible cylinders subject to vortex-induced vibrations". *Journal of Fluid Mechanics, 400*, pp. 91–124.

[6] Grouthier, C., Michelin, S., Bourguet, R., Modarres-Sadeghi, Y., and De Langre, E., 2014. "On the efficiency of energy harvesting using vortex-induced vibrations of cables". *Journal of Fluids and Structures, 49*, pp. 427–440.

[7] Aswathy, M., and Sarkar, S., 2019. "Effect of stochastic parametric noise on vortex induced vibrations". *International Journal of Mechanical Sciences, 153*, pp. 103–118.

[8] Denoël, V., 2020. "Derivation of a slow phase model of vortex-induced vibrations for smooth and turbulent oncoming flows". *Journal of Fluids and Structures, 99*, p. 103145.

[9] Shoshani, O., 2018. "Deterministic and stochastic analyses of the lock-in phenomenon in vortex-induced vibrations". *Journal of Sound and Vibration, 434*, pp. 17–27.

[10] Aswathy, M., and Sarkar, S., 2021. "Frequency characteristics and phase dynamics of a stochastic vortex induced vibration system". *Journal of Sound and Vibration, 509*, p. 116230.

[11] Facchinetti, M. L., De Langre, E., and Biolley, F., 2004. "Coupling of structure and wake oscillators in vortex-induced vibrations". *Journal of Fluids and Structures, 19*(2), pp. 123–140.

[12] Srinil, N., and Zanganeh, H., 2012. "Modelling of coupled cross-flow/in-line vortex-induced vibrations using double duffing and van der pol oscillators". *Ocean Engineering, 53*, pp. 83–97.

[13] Opinel, P.-A., and Srinil, N., 2020. "Application of wake oscillators to two-dimensional vortex-induced vibrations of circular cylinders in oscillatory flows". *Journal of Fluids and Structures, 96*, p. 103040.

[14] Krenk, S., and Nielsen, S. R., 1999. "Energy balanced double oscillator model for vortex-induced vibrations". *Journal of Engineering Mechanics, 125*(3), pp. 263–271.

[15] Nielsen, S. R., and Krenk, S., 1997. "Stochastic response of energy balanced model for vortex-induced vibration".

[16] Bayram, M., Partal, T., and Orucova Buyukoz, G., 2018. "Numerical methods for simulation of stochastic differential equations". *Advances in Difference Equations, 2018*(1), pp. 1–10.

[17] Khalak, A., and Williamson, C., 1996. "Dynamics of a hydroelastic cylinder with very low mass and damping". *Journal of fluids and structures, 10*(5), pp. 455–472.

[18] Pastò, S., 2008. "Vortex-induced vibrations of a circular cylinder in laminar and turbulent flows". *Journal of Fluids and structures, 24*(7), pp. 977–993.